Projections of snow water equivalent using a process-based energy balance snow model in southwestern British Columbia

Stephen R. Sobie, Trevor Q. Murdock

2022

Original citation:

Sobie, S. R., & Murdock, T. Q. (2022). Projections of snow water equivalent using a process-based energy balance snow model in southwestern British Columbia. *Journal of Applied Meteorology and Climatology, 61*(1), 77–95. https://doi.org/10.1175/JAMC-D-20-0260.1

Projections of Snow Water Equivalent Using a Process-Based Energy Balance Snow Model in Southwestern British Columbia

STEPHEN R. SOBIE[a] AND TREVOR Q. MURDOCK[a]

[a] *Pacific Climate Impacts Consortium, University of Victoria, Victoria, British Columbia*

(Manuscript received 20 November 2020, in final form 15 September 2021)

ABSTRACT: Information about snow water equivalent in southwestern British Columbia, Canada, is used for flood management, agriculture, fisheries, and water resource planning. This study evaluates whether a process-based, energy balance snow model supplied with high-resolution statistically downscaled temperature and precipitation data can effectively simulate snow water equivalent (SWE) in the mountainous terrain of this region. Daily values of SWE from 1951 to 2018 are simulated at 1-km resolution and evaluated using a reanalysis SWE product [Snow Data Assimilation System (SNODAS)], manual snow-survey measurements at 41 sites, and automated snow pillows at six locations in the study region. Simulated SWE matches observed interannual variability well ($R^2 > 0.8$ for annual maximum SWE), but peak SWE biases of 20%–40% occur at some sites in the study domain, and higher biases occur where observed SWE is very low. Modeled SWE displays lower bias relative to SNODAS reanalysis at most manual survey locations. Future projections for the study area are produced using 12 downscaled climate model simulations and are used to illustrate the impacts of climate change on SWE at 1°, 2°, and 3°C of warming. Model results are used to quantify spring SWE changes at different elevations of the Whistler mountain ski resort and the sensitivity of annual peak SWE in the Metropolitan Vancouver municipal watersheds to moderate temperature increases. The results both illustrate the potential utility of a process-based snow model and identify areas where the input meteorological variables could be improved.

SIGNIFICANCE STATEMENT: Using high-resolution (1 km) climate data, we evaluate and apply a snow model in the mountainous terrain of coastal, southwestern British Columbia, Canada. Modeling snow water equivalent at high-resolution enables better representation of snow conditions that can vary widely over short distances and elevations. At 1°, 2°, and 3°C of warming, future snow water equivalent levels at sites nearer the coast are more vulnerable to temperature increases than sites slightly higher in elevation and farther inland. Future efforts to improve the climate data may yield better agreement between simulated and observed snow levels in certain locations.

KEYWORDS: Complex terrain; Snowpack; Climate change

1. Introduction

Spatially distributed, high-resolution information about snowpack is important for natural resources and human activity in southwestern British Columbia, Canada. Seasonal and annual variations in snow accumulation affect the movement and storage of water on the landscape with a variety of subsequent effects. Hydroelectric power generation reservoirs and urban drinking water sources are commonly supplied by hybrid (mixed rain and snow) watersheds where melting snowpack in summer is key to maintaining water levels (Barnett et al. 2005; Pinna Sustainability 2016). Ski and other winter recreational resorts located at relatively low elevations can suffer shortened or lost seasons during warmer winters (Scott and McBoyle 2006; Municipality of Whistler 2016). Salmon and other fish species depend on melting snow to maintain both sufficient water depth and cold temperature for survival (Morrison et al. 2002). Effective flood control on the Fraser River requires detailed information about snow conditions in the mountainous tributaries of the river (Curry and Zwiers 2018). The ability to simulate snow water equivalent levels accurately throughout this region is necessary for quantifying potential impacts and understanding future evolution of snow in a changing climate.

Existing efforts to simulate snow water equivalent (SWE) range from simple temperature index models to computationally expensive regional climate models. Temperature index models offer simplicity, with snow accumulation and melt factors normally based on thresholds or degree-days from daily temperatures (Bormann et al. 2014; Ohmura 2001). Index models are used in flood forecast applications in British Columbia (BC) where time efficiency is a priority (Luo 2017) and can perform well in homogeneous regions (Kumar et al. 2013), given sufficient observations of snow to calibrate melt factors correctly. Hydrologic modeling in BC and the Pacific Northwest often involves distributed modeling of SWE, where the simulation of snowpack is required to model streamflow accurately (Curry and Zwiers 2018; Pomeroy et al. 2007; Garen and Marks 2005). Hydrologic models have identified decreases in soil moisture caused by shorter snow seasons, reduced spring snowpack, and earlier melt combined with warmer, drier summers as a result of a changing climate leads to increase fire potential in the western United States (Gergel et al. 2017). More detailed representations of SWE can be obtained from land surface models used in reanalysis products (Mudryk et al. 2015) and regional climate models (Frei et al. 2018) operating at increasingly fine resolution (Liu

Denotes content that is immediately available upon publication as open access.

Corresponding author: Stephen R. Sobie, ssobie@uvic.ca

DOI: 10.1175/JAMC-D-20-0260.1

et al. 2017) that include multiple snow layers and internally consistent relationships between temperature and precipitation. This enables exploration of coincident events such as rain-on-snow that are expected to increase in frequency with future warming resulting in accelerated snowmelt and flooding during winter and spring in western North America (Il Jeong and Sushama 2018). Recently, machine-learning (ML) techniques have shown positive results in estimating SWE in BC using remote sensing and ground-based SWE products as predictors (Snauffer et al. 2018) and will likely become more commonplace as saliency techniques improve. Depending on the modeling framework used, however, these latter methods can require considerable computational resources, limiting the length and number of simulations possible.

The SWE modeling approach employed in this analysis is a process-based, energy balance snow model (Walter et al. 2005, herein the Walter snow model). Process-based snow models such as SnowModel (Liston and Elder 2006), image snowcover energy and mass-balance model (ISNOBAL; Marks et al. 1999), and others (Rutter et al. 2009) calculate daily quantities of SWE following parameterized atmospheric, energy, and mass components. The models include options for multiple snow layers, thermodynamics, and detailed internal snow structure, along with a range of potential meteorological inputs (Rutter et al. 2009). SnowModel is a calibrated SWE model including four submodel components responsible for high-resolution meteorological conditions, snowpack energy balance, snow transport and sublimation from wind, and mass exchange in a single snowpack layer. SnowModel has been applied in a range of snow environments (Liston and Elder 2006) and has been effective in quantifying the vulnerability of maritime SWE above 1000 m at 2°C temperature increase the western United States (Sproles et al. 2013). ISNOBAL is an uncalibrated model representing SWE with a multilayer mass and energy balance snow model (Marks et al. 1999) and has been applied successfully to basins across western North America (Kumar et al. 2013). Unlike SnowModel, ISNOBAL lacks representation of canopy effects on snow storage and radiation and requires additional inputs of radiation and soil temperature. The Walter snow model is similar in concept to ISNOBAL but requires fewer inputs (daily temperature, precipitation, and geographical information) that better match data availability in the region and is simpler in design than ISNOBAL and SnowModel. Daily accumulation and ablation of SWE in a single snow layer is affected by external radiation and heat transfer, with each distributed cell within the model operating independently (no wind transport). The model can be applied rapidly for any domain at any specified resolution, with parameterizations and constants taken from the literature (Walter et al. 2005). Simplified physical representations in the Walter snow model also means many simulations can be produced more rapidly, enabling the analysis of future climate impacts using an ensemble of future climate models.

Snow-model performance is constrained in large part by the quality of input data supplied to the models (Rutter et al. 2009; Garen and Marks 2005). If biases in the meteorological data are reduced, a simpler snow model may perform effectively at simulating daily SWE without requiring a more detailed and computationally costly model such as SnowModel (Liston and Elder 2006). The goal of this study is to evaluate the performance of the Walter snow model in simulating SWE in southwestern British Columbia by leveraging high-resolution statistically downscaled meteorological variables (Sobie and Murdock 2017). How well this model simulates present day daily SWE is judged using manual and automated SWE measurements and a reanalysis SWE dataset. As part of the snow-model implementation, a revised rain–snow phase partitioning method is added that is calibrated using the manual and automated SWE measurements. Calibration is limited to the rain–snow phase component only, so as to evaluate the model in its present configuration and limit the extent of model tuning. The snow model is then applied with inputs from 12 future climate simulations to investigate how future snow amounts are expected to change in the study area.

Particular focus in the model evaluation and future projections is directed to average spring SWE and annual peak SWE, with results given for two applications. Spring SWE provides information about the peak and melting periods of the snow season and can determine at what elevation and for how long ski slopes can operate (Damm et al. 2017). Future projections of average spring SWE are presented at the location of Whistler–Blackcomb Ski Resort in the Coast Mountains. Annual maximum SWE values serve both as an indicator of stored water in the snowpack and as a test of whether the model is correctly integrating precipitation, temperature, and snow phase over the accumulation part of the snow season. Future projections of annual peak SWE are calculated for three watersheds used to supply municipal drinking water for Metropolitan Vancouver (hereinafter Metro Vancouver). Here, infrequent summer precipitation and low elevation of the watersheds means water reservoirs are dependent on melting snowpack that is vulnerable to increasing temperatures (Metro Vancouver Water Services 2011).

2. Data

a. Study area

The study region consists of southwest, mainland British Columbia, an area of 46 100 km^2 (Fig. 1). Highly varying topography including the southwestern extent of the Coast Mountain range (from sea level to nearly 3000-m elevation) and major river basins (Cheakamus, Fraser, Lillooet, and Squamish) as well as urban, forested, and alpine terrain are all contained within the domain. Annual precipitation ranges from 200 to over 5000 mm and primarily occurs in November–January. Moderation from the Pacific Ocean leads to winter temperatures frequently near 0°C and frequently changing precipitation phases, even at high elevations. Timing of the spring freshet on local rivers, important for agriculture and flood management, generally occurs between mid-May and July and is dependent on antecedent mountain snow conditions.

b. Snow-survey and snow-pillow observations

Observations of snow water equivalent were obtained for 47 locations in southwestern BC (Fig. 1) from the BC Ministry of Environment and Climate Change Strategy (BC Ministry of Environment and Climate Change Strategy 2015). Forty-one of

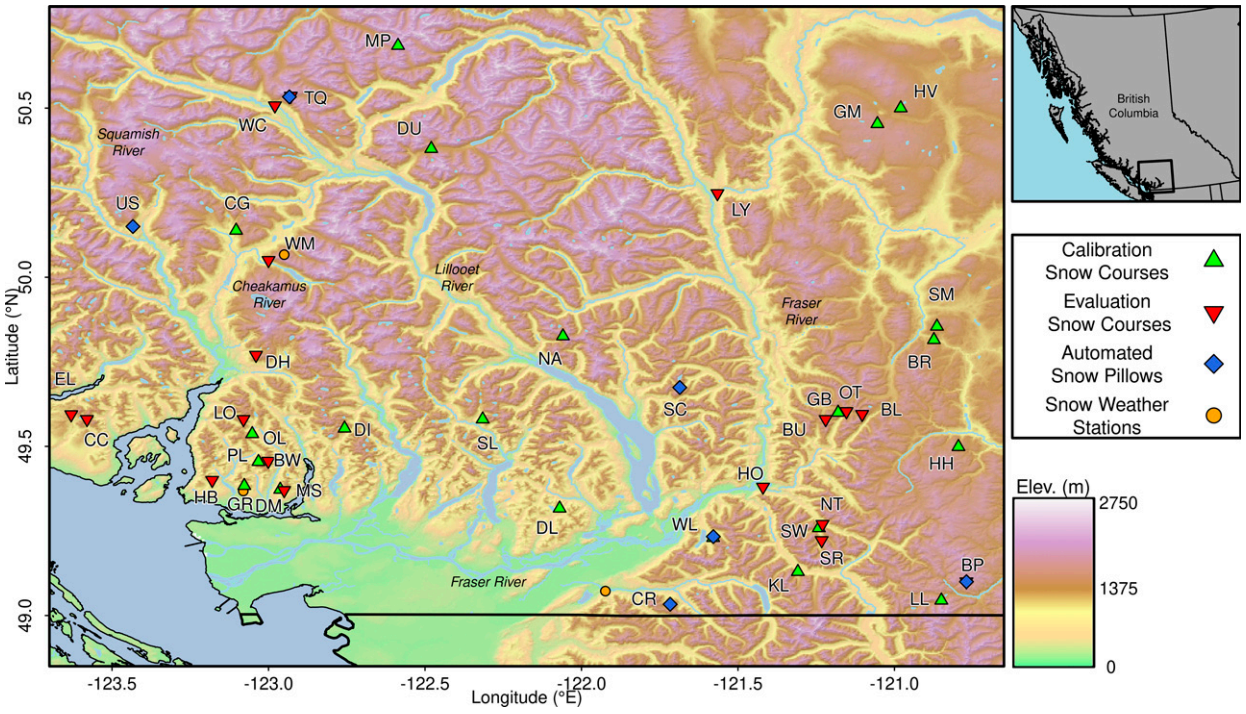

FIG. 1. Study-area map of southwestern British Columbia with elevation and snow-survey and snow-pillow locations identified. Manual survey sites are marked by green (calibration) and red (evaluation) triangles, and automated survey sites are marked by diamonds. Station names and elevations are provided in Tables A1 and A2 in appendix A. Weather stations used to illustrate snowfall occurrence are marked by orange circles, and the coordinates are provided in Table 3, below.

the locations are manual snow surveys operated by the BC Snow Survey Program that typically record measurements 1–6 times per year and are the average of multiple measurements taken at each location and time. The manual snow-survey observations are divided into 21 calibration and 20 evaluation sites. All calibration sites have at least 30 years of measurements, whereas most of the evaluation site records are shorter with some observation gaps. The remaining six locations are automated snow-pillow (ASP) observations, which are shorter in length, from 18 to 35 years, but measure daily throughout the year. These snow-pillow sites also include some observations of daily temperature (although with gaps in the records). Site names, map symbols, and site elevations are provided in appendix A.

c. *SNODAS*

Daily, gridded values of snow water equivalent were obtained from the National Oceanic and Atmospheric Administration (NOAA) Snow Data Assimilation System (SNODAS; National Operational Hydrologic Remote Sensing Center 2004; Barrett 2003). SNODAS spatially distributed 30-arc-s SWE is generated using an energy and mass balance snow model (National Operational Hydrologic Remote Sensing Center Snow Model). Meteorological inputs are downscaled from simulations of the Rapid Update Cycle (RUC2, prior to September 2018) and Rapid Refresh (RAP, since September 2018) numerical weather prediction models constrained by ground (primarily ASPs in Canada), airborne and satellite observations. SWE is available for southern Canada from December 2009 to present.

d. *Snow-model climate data*

The process-based snow model used in this study requires inputs of daily maximum and minimum temperature, and daily precipitation, which were obtained from two historical climate datasets for model evaluation and from a set of 12 downscaled global climate models for past and future simulations. Evaluation of the snow-model performance relative to observed SWE was performed with two historical simulations; one using meteorological inputs from the Pacific Climate Impacts Consortium Meteorology for Northwest North America gridded observational dataset spanning 1945–2012 (PNWNAmet; Werner et al. 2019) and another using inputs from the ERA5 reanalysis dataset spanning 1980–2018 (Hersbach et al. 2018; Copernicus Climate Change Service 2017). Gridded observations in PNWNAmet are obtained by interpolating quality-controlled weather-station data from Environment and Climate Change Canada using thin-plate splines guided by geographic and high-resolution climate normal The resulting daily dataset covers western North America at 1/16° resolution.

Past and future simulations of temperature and precipitation were obtained from 12 global climate models (GCMs) of varying resolutions spanning 1951–2100 generated from phase 5 of the Coupled Model Intercomparison Project (CMIP5; Taylor et al. 2011) provided via the Earth System Grid

TABLE 1. Energy balance variables for the snow model used in this study.

Variable	Symbol	Definition	Components
Solar radiation	S	$S = (1 - A)T_tS_o$	A: albedo; T_t: atmospheric transmissivity; S_o: potential solar radiation
Atmospheric longwave radiation	L_a	$L = \varepsilon_a\sigma T_a^4$	ε_a: atmospheric emissivity; σ: Stefan–Boltzmann constant; T_a: air temperature
Terrestrial longwave radiation	L_t	$L = \varepsilon_s\sigma T_t^4$	ε_s: surface emissivity; σ: Stefan–Boltzmann constant; T_t: snow temperature
Sensible heat exchange	H	$H = \frac{C_a(T_s - T_a)}{r_h}$	C_a: heat capacity of air; T_s: snow temperature; T_a: air temperature; r_h: resistivity to heat transfer
Heat from convective vapor exchange	E	$E = \frac{\lambda_v(\rho_s - \rho_a)}{r_v}$	λ_v: latent heat of vaporization; ρ_s: vapor density at surface; ρ_a: vapor density in air; r_v: resistance to vapor exchange
Heat advection from rainfall	P	$P = C_wR_pT_a$	C_w: heat capacity of water; R_p: depth of rain; T_a: air temperature
Ground heat conduction	G	173 kJ m^{-2}	U.S. Army Corps of Engineers melt estimate

Federation (Williams et al. 2009). The 12 GCMs (appendix B) were selected following Cannon (2014) to be a representative subset from the much larger CMIP5 ensemble of GCMs to reduce computational costs while retaining as much information from the ensemble as possible. Models employing the highest concentration pathway, RCP8.5 (Riahi et al. 2011) were selected to generate future climate projections.

To achieve the high-resolution inputs required for the snow model, coarse-scale fields from ERA5 and each of the 12 GCMs were statistically downscaled using a two-stage approach (Sobie and Murdock 2017). First, daily temperature and precipitation values were downscaled to a medium resolution of 1/16° using bias correction constructed analogs with quantile mapping, version 2 (BCCAQv2; Werner and Cannon 2016; Cannon et al. 2015), using PNWNAmet for calibration. BCCAQv2 incorporates quantile delta mapping to preserve relative changes from the coarse fields, which reduces potential inflationary effects when standard quantile mapping is used (Maraun 2013). Second, the 1/16° output from the first stage is then downscaled to 1/120° (30 arc s or approximately 1 km) by climate imprint bias correction (Hunter and Meentemeyer 2005) using monthly observed climate normals for 1981–2010 produced with the Parameter–Elevation Regressions on Independent Slopes Model (PRISM; Daly et al. 2008). Combining downscaling with BCCAQv2 and bias-correction with PRISM climatologies yields better representation of temperature and precipitations patterns, particularly at high elevation (Sobie and Murdock 2017). For the historical snow-model evaluation, PNWNAmet fields are also downscaled from 1/16° to 1/120° using the same second stage bias correction method before use with the snow model. A complete description of the downscaling process is provided in Sobie and Murdock (2017).

3. Process-based energy balance snow model formulation

The Walter snow model is an energy-balance model that incorporates physically based representations of contributory processes to snowmelt through a set of parameterizations (Walter et al. 2005). Definitions of the main model parameters are listed in Table 1, with full explanations of the secondary variables given in Walter et al. (2005). The snow model is implemented within the R package "EcoHydRology" (Fuka et al. 2018).

The snow model tabulates different components to the energy balance [Eq. (1)] at a daily time step based on daily maximum and minimum temperature, daily total precipitation, day of the year, latitude, and slope angle and aspect to determine how much snow water equivalent is accumulated or lost. In each model cell on the ith day, the single snow layer energy balance EB_i is governed by solar (S_i), atmospheric ($L_{a,i}$), and terrestrial ($L_{t,i}$) radiation; sensible (H_i) and latent (E_i) exchange of heat with the atmosphere; and sensible heat exchange both with rainfall (P_i) and the land surface underneath (G):

$$EB_i = S_i + L_{a,i} - L_{t,i} + H_i + E_i + P_i + G. \quad (1)$$

Intensity of solar radiation absorbed by the surface layer is determined by the angle of the local surface to the sun, the surface albedo A, and the atmospheric transmissivity T_t. Local solar declination angle set by the latitude and time of the year is modulated by the topographic slope and aspect values for each grid cell calculated from the PRISM digital elevation model used by the snow model. Surface albedo ranges from a maximum of 0.95 for fresh snow and decays temporally in the absence of new snowfall to a minimum of 0.25 for bare ground. Atmospheric transmissivity is determined using an empirical equation dependent on season, location, and diurnal temperature range. Atmospheric (L_a)

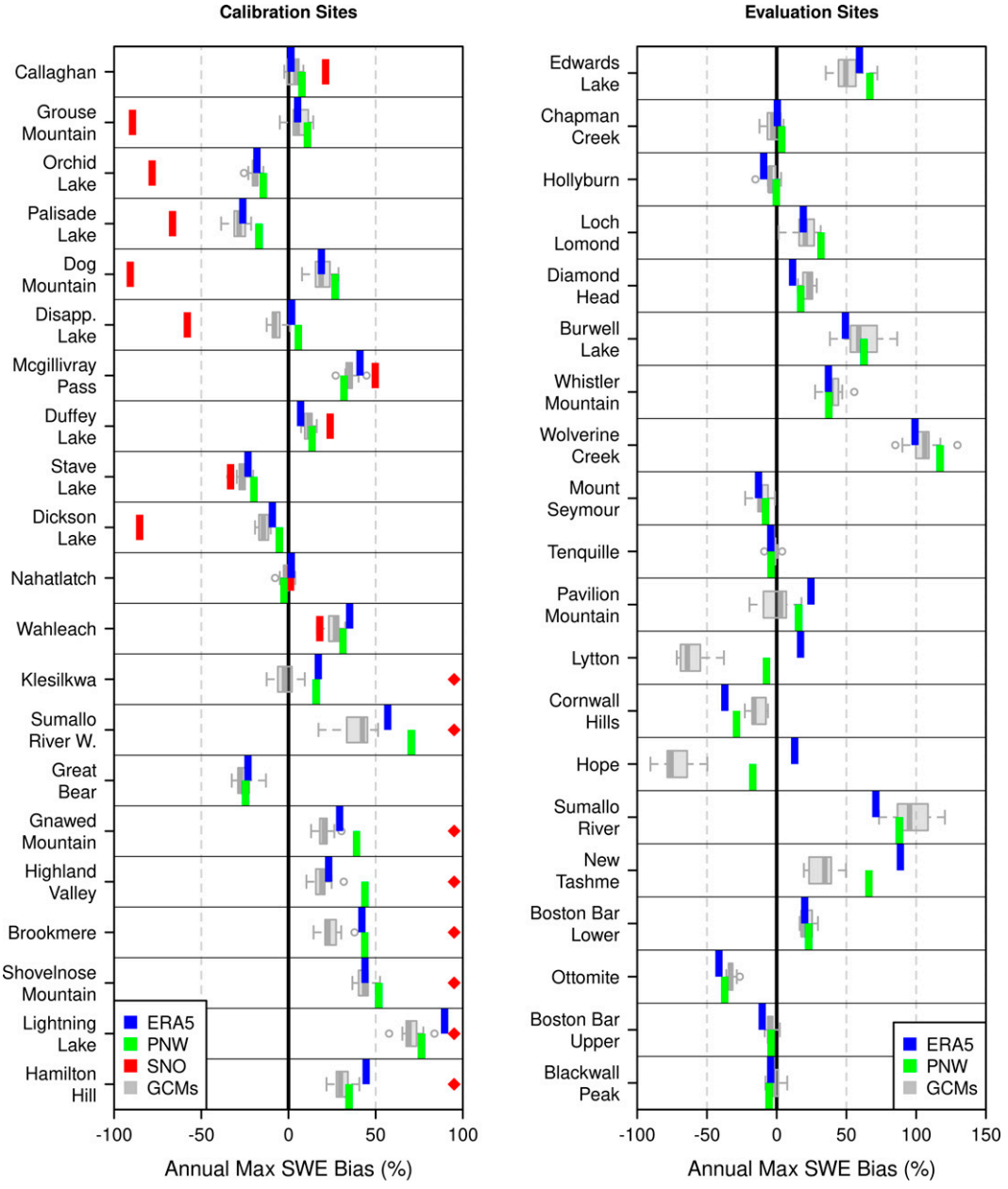

FIG. 2. Annual maximum biases relative to annual maximum SWE [100(model − observation)/observation] between model simulated SWE, SNODAS SWE, and observed SWE at all snow-survey locations. Historical simulations of model SWE using inputs from gridded observations between 1951 and 2012 (PNWNAmet; green), reanalysis between 1980 and 2018 (ERA5; blue), and historical GCM simulations between 1951 and 2005 (gray boxplots) are compared with all corresponding dates of observed SWE. SNODAS SWE (red) is compared over the period between 2009 and 2018. Where SNODAS bias is greater than 100% is indicated by red diamonds at the right of the panel. (left) Sites used to calibrate the parameters of the snow phase equation with PNWNAmet; (right) bias for sites excluded from the calibration step. SNODAS is excluded from the right panel (and Great Bear in the left panel) because the short record available does not overlap with most of the evaluation-site observations. Sites are ordered by longitude from west to east.

and terrestrial (L_t) emission of radiation is assumed to follow the graybody form of the Stefan–Boltzmann equation with atmospheric emissivity determined primarily by cloud cover (inferred from precipitation occurrence), and snow emissivity is held at a constant value (0.97).

Sensible heat flux H between the snow layer and the atmosphere is proportional to the temperature difference between the atmosphere and the snow surface, limited by resistance to heat transfer r_h, which is assumed to depend primarily on the wind speed at the surface. Surface wind speed also determines

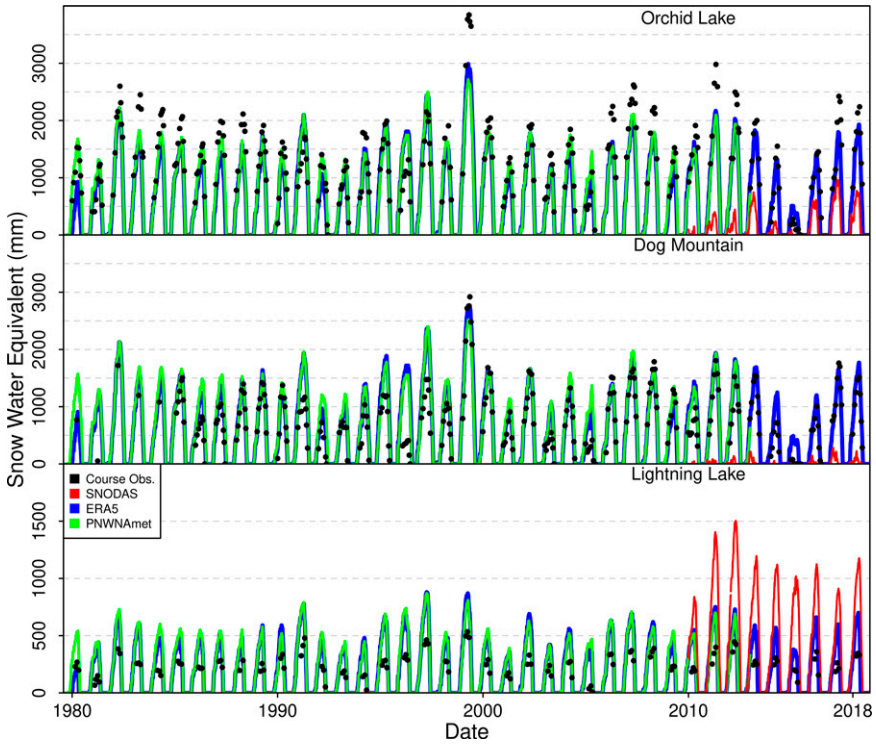

FIG. 3. Time series of modeled SWE between 1980 and 2018 at the (top) Orchid Lake, (middle) Dog Mountain, and (bottom) Lightning Lake manual snow-survey (snow course) sites using inputs from PNWNAmet (green) and ERA5 (blue). Overlapping observations of snow-course SWE are displayed as black dots, and reanalysis SNODAS SWE (2009–18) is displayed in red.

resistance to vapor exchange r_v in the exchange of latent heat due to vaporization and condensation in the snow layer, which is proportional to the difference in atmosphere and surface vapor density. Because humidity is not available in the downscaled simulations, vapor density is calculated using minimum temperature in place of dewpoint temperature. Similarly, given the unavailability of wind in the downscaled simulations, wind speeds were assumed constant at 2 m s^{-1} (estimated from PNWNAmet annual mean wind speeds) over the study area for both resistance terms. Sensible heat transfer G from the ground beneath the snow layer is assumed constant (and relatively small when compared with the other components) based on estimated values from the U.S. Army Corps of Engineers (1998). Land-cover differences, specifically, tree canopy coverage, are not explicitly included in the model leading to simplified versions of these exchanges at the surface. Precipitation falling as rain (assumed to be at the atmospheric temperature) adds further energy P equal to that released by reducing the rainfall temperature to freezing.

The energy balance equation EB determines the amount of melt M that must occur to change the energy content of the snow water equivalent in the snow model [Eq. (2)]. Snow water equivalent on the ith day (SWE_i) is the sum of any previous snow water equivalent (SWE_{i-1}) plus any new snow N_i reduced by losses due to melt M_i [Eq. (3)]. Snowmelt on the ith day (M_i) is the difference between the energy balance EB_i and the energy required to warm the existing snow ($SWE_{i-1} + N_i$), where C_s is the heat capacity of snow, ρ_w is the density of water, L_f is the latent heat of freezing, and $T_{s,i}$ is the snow temperature (°C). Snow temperature decreases and increases proportionally to net energy changes EB_{i-1}, to a maximum of 0°C. Negative values of snowmelt (possible due to terrestrial longwave radiative cooling) are treated as zero losses:

$$M_i = \frac{\mathrm{EB}_i - C_s(\mathrm{SWE}_{i-1} + N_i)\rho_w|T_{s,i}|}{L_f\rho_w} \quad \text{and} \tag{2}$$

$$\mathrm{SWE}_i = \mathrm{SWE}_{i-1} + N_i - M_i. \tag{3}$$

New snow water equivalent N_i is accumulated by precipitation defined as snow according to the conditional snow frequency [Eq. (4)]. In the model's default configuration, the fraction of daily total precipitation considered snow is defined as any precipitation that falls when the daily average temperature is less than zero. This is redefined to allow some snow to occur when daily average temperatures are above 0°C (Dai 2008) reflecting what is observed in study-area weather-station observations (Jennings et al. 2018):

$$F_s(T_a) = a\{\tanh[b(T_a - c)] - d\}. \tag{4}$$

Snow phase fraction F_s is determined using a hyperbolic tangent function [Eq. (4)] of daily average temperature T_a adapted from Dai (2008). The four parameters of the function

TABLE 2. Differences in reported snow-survey or ASP elevation and the elevation of the nearest PRISM DEM cell for selected snow-observing sites. Average temperature differences (DEM − site) are calculated by applying the elevation difference to temperature lapse rates from PRISM. Lapse rates are estimated using PRISM climatologies from the 25 cells surrounding the nearest grid cell (applying a two-cell buffer to the nearest cell).

Site name	Site elev (m)	DEM elev (m)	DEM − site diff (m)	Temperature diff (°C)
Grouse Mountain	1126	1061	−65	0.35
Orchid Lake	1178	1079	−99	0.58
Palisade Lake	898	816	−82	0.56
Dog Mountain	1080	1009	−71	0.40
Mcgillivray	1725	1900	175	−1.0
Stave Lake	1211	1154	−57	0.33
Spuzzum	1197	1279	82	−0.54
Great Bear	1660	1536	−124	0.78
Lightning	1254	1324	70	−0.36
Edwards	1070	1082	12	−0.05
Burwell	880	915	35	−0.17
New Tashme	700	804	104	−0.44
Ottomite	1460	1206	−254	1.75
Sumallo River	880	937	57	−0.24
Wolverine Creek	250	284	34	−0.15

denote the scaling factor (a, controlling the point at which the fraction of precipitation considered to be snowfall is less than 1), slope (b, setting how quickly the snow–rain fraction shifts from all snow to all rain), half-frequency point (c, approximately the point at which snow and rain occur at equal frequencies), and the symmetry parameter (d, allowing for asymmetry at large negative and positive temperatures).

Precipitation on the ith day Pr_i is then partitioned into new snow water equivalent N_i and rainfall R_i according to the snow phase fraction $F_{s,i}(T_{a,i})$:

$$N_i(\mathrm{Pr}_i, T_{a,i}) = \mathrm{Pr}_i F_{s,i}(T_{a,i}) \quad \text{and} \tag{5}$$

$$R_i(\mathrm{Pr}_i, T_{a,i}) = \mathrm{Pr}_i\left[1 - F_{s,i}(T_{a,i})\right]. \tag{6}$$

Site-specific snow phase function parameters are obtained by calibrating the snow model at the 21 calibration manual snow-survey and 6 snow-pillow locations. Observations of SWE at each site are divided into two equal subsets, and each is used alternately for calibration and evaluation. Parameters a, b, and c in Eq. (4) are calibrated in each subset by selecting values within specified bounds that minimize the root-mean-square error between observed SWE and model simulated SWE using precipitation and temperature from PNWNAmet bias-corrected with PRISM. Parameter bounds are developed from the ranges in Dai (2008). The scaling parameter a spans from −52 to −48, increasing values of which shift the point of precipitation being 100% snowfall to more negative temperatures. The slope parameter b spans 0.25°–1.25°C^{-1}, which increases the rapidity of the phase transition. The half-frequency point c (spanning 1.5°–4.5°C) denotes the temperature where snow and rain fractions are approximately equal. The symmetry parameter d was found to vary minimally during the calibration process and was set to be 1.0209 obtained from the least squares estimates for winter (December–February) over land in Dai (2008). Further examples of the effect that each phase equation parameter has on the resulting $F_s(T_a)$ curve can be seen in Dai (2008). Snow phase parameters from the two calibration subsets are averaged at each site and then interpolated to 30-arc-s resolution across the entire study area using thin-plate spline interpolation (Nychka et al. 2017) with elevation as a covariate to account for the highly varying topography in the study area.

4. Results

a. Snow-model evaluation

Performance of the process-based snow model is evaluated at each of the 47 SWE observation sites using historical simulated SWE. At each location, simulated SWE is produced using precipitation and temperature from PNWNAmet (1945–2012). Snow simulations using ERA5 (1980–2018) are also generated using snow phase parameters calibrated with PNWNAmet. At each of the 27 calibration sites, performance metrics are displayed from the periods excluded from the calibration with PNWNAmet. As each of the calibration sites have at least 30 years of observations, the two evaluation periods include at least 15 years though the number of years can vary depending on the site.

Snow-model SWE bias in annual maximum SWE at the observation sites is displayed in Fig. 2 in order from west to east. Annual maximum SWE bias is defined as the difference between the modeled and observed annual maximum SWE relative to the average annual maximum observed SWE multiplied by 100%. Simulated SWE bias is less than 40% at most of the calibration sites, with the largest differences at sites with the lowest average maximum SWE (e.g., Sumallo River West at 160 mm, Shovelnose Mountain at 180 mm, and Lightning Lake at 290 mm). Reasons for bias amounts can vary between nearby observation sites. For example, at Orchid Lake in the North Shore Mountains, modeled SWE is systematically underestimated in most years by 15%–22% (230–340 mm) (Fig. 3). Here, the model grid cell for Orchid Lake exists

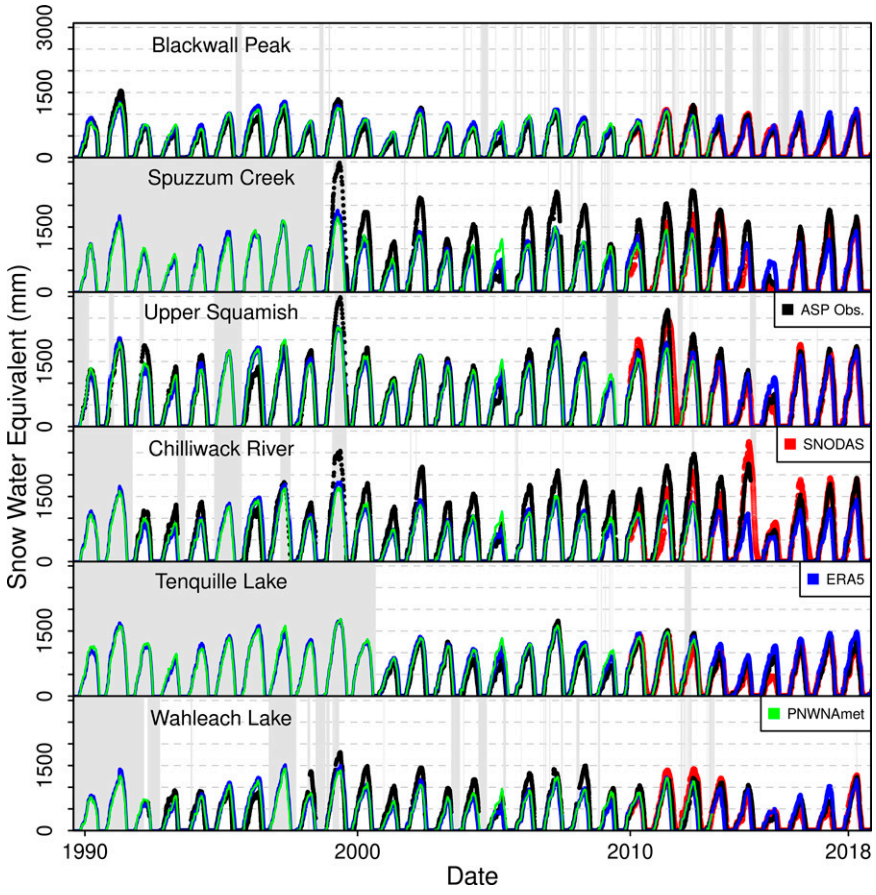

FIG. 4. Daily snow water equivalent at the six ASP locations from the snow-pillow observations (black), snow-model simulations (PNWNAmet: green; ERA5: blue) and SNODAS SWE (red). SNODAS SWE observations are only available after 2009. Dates for which ASP observations are missing are shown by gray vertical lines.

100 m below that of the snow-survey reported elevation. Temperature lapse rates estimated from the PRISM digital elevation model (DEM) and PRISM temperature climatologies at cells surrounding the site suggest this results in a 0.6°C warm temperature bias (Table 2) that likely decreases the fraction of precipitation as snow in each year. Similar warm temperature biases and underestimation of annual maximum SWE are present at Palisade Lake, Stave Lake, and Great Bear.

The opposite effect is evident at Lightning Lake, where a 75%–90% (225–270 mm) positive bias occurs at a model cell located 70 m above the elevation of the snow survey. At Dog Mountain just to the south of Orchid Lake, the 25% (300 mm) positive bias arises mainly from a few individual years in which observed SWE is very low and modeled SWE is substantially overestimated (Fig. 3). Most other years are largely modeled correctly, suggesting precipitation from the gridded observations may be too high, or the fraction of precipitation assigned as snow may be too large, for those individual years at this site. Biases in peak SWE from the 12 historical downscaled GCMs is largely similar to those from the PNWNAmet and ERA5 SWE, with GCM biases being generally more negative. Differences between PNWNAmet and ERA5 SWE biases occur at some sites but vary in magnitude by location, without any systematic pattern of difference among the sites. At snow-survey sites where modeled SWE bias is large, the bias of SNODAS for those same sites appears to be much larger, likely as a result of the apparent exclusion of Canadian manual snow-survey observations from the SNODAS assimilation process. For all survey sites from Klesilkwa eastward, SNODAS SWE bias is over 100% greater than observed peak SWE.

Evaluation sites where the snow model exhibits the largest bias (Fig. 2; right panel) also tend to be those with the low peak SWE such as Wolverine Creek (110 mm), Sumallo River (260 mm), and New Tashme (275 mm). These sites are also located in narrow valley bottoms close to steep terrain and occur at elevations between 30 and 100 m higher in the PRISM DEM than the reported site elevations, likely leading to an overestimation of precipitation as snow (Table 2). Lower SWE levels are also missed by the historical GCM SWE at Hope (90 mm) and Lytton (30 mm), suggesting the GCM SWE may not capture low elevation, marginal SWE correctly.

Modeled SWE tracks the interannual variability of observed SWE very well (coefficient of variation R^2 between 0.85 and 0.97 for annual maximum SWE) but underestimates

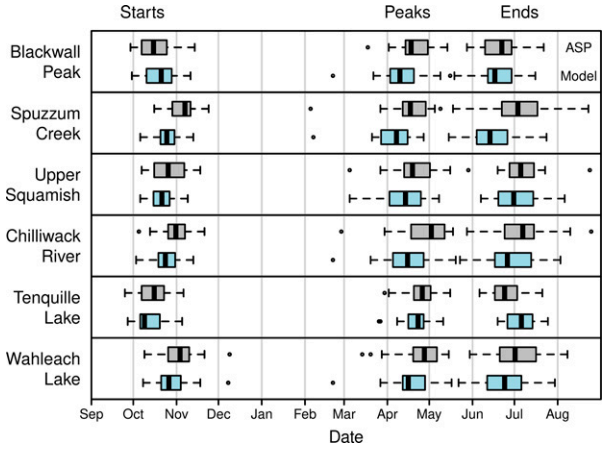

FIG. 5. Snow-season start, peak, and end dates for each of the ASP observational sites. The snow season is defined as days of the year with SWE > 10 mm. Simulated snow-season dates are calculated from the model years corresponding to the years observed by the ASPs. Model statistics are drawn from the both the PNWNAmet and ERA5 snow-model simulations at each site. Individual boxplots display the median (central line), interquartile range (central box), 1.5 times the interquartile range (whiskers), and outliers beyond the whiskers (open circles).

the annual accumulated SWE at Spuzzum Creek, Chilliwack River, and certain years in the other automated snow-pillow locations (Fig. 4). During the anomalously wet and cold winters of 1998/99 and 2011/12, both PNWNAmet and ERA5 datasets have insufficient precipitation to accumulate the observed SWE, even if all precipitation is considered snow (not shown). At all six ASP locations there is effectively no difference in the performance between the PNWNAmet and ERA5 SWE simulations. For the nine years of available SNODAS SWE there is close agreement between SNODAS and snow-pillow values reflecting the inclusion of snow-pillow observations (unlike the snow surveys) as part of the observational assimilation process in SNODAS.

Snow-season (days of the year with SWE > 10 mm) timing is also useful in determining time-dependent events such as the spring freshet, even if the magnitudes of SWE are not simulated perfectly. Snow-season timing in each year (start dates, peak dates, end dates, and lengths) is replicated well by the snow model (Fig. 5). The dates and lengths (obtained from all years in the observations or modeled SWE) span similar ranges between the simulated SWE and ASP values. Modeled snow seasons tend to start earlier (by 2–12 days), peak earlier (by 1–13 days), and end earlier (by 1–18 days) than occurs in the observed SWE records (except for the start date at Blackwall Peak and the end date at Tenquille Lake) and span similar lengths.

Coincident observed measurements of snow water equivalent, temperature, and precipitation are rare, making the direct evaluation of snow-model sensitivity to input meteorological variables difficult. Limited records of daily average temperature are available at the six automated snow-pillow locations, albeit with periods of missing data. At Spuzzum Creek and Chilliwack River, where snow-model SWE is lower than observed, PNWNAmet temperatures are warmer by 0.44° and 0.72°C, respectively, on average between 1993 and 2012. The slightly too warm temperatures supplied to the snow model could explain the systematic underestimation of SWE at these sites, but these limited temperature measurements have not been subject to quality control or homogenization and must be interpreted cautiously. Temperature biases at the four other pillow sites are between −0.22° and 0.19°C.

TABLE 3. Location, elevation, and time interval information for the Environment and Climate Change Canada weather stations used for daily snowfall evaluation.

Site name	Lon	Lat	Elev (m)	Obs time
Chilliwack	121.925°W	49.172°N	11	1981–2011
Grouse	123.081°W	49.368°N	1128	1981–2011
Whistler	122.955°W	50.129°N	658	1981–2011

b. *Snow phase fraction evaluation*

Simulated daily snowfall is evaluated by examining the snow phase fraction component of the snow model. Modeled precipitation occurrence designated as snowfall by Eqs. (4) and (5) is sorted by its coincident daily average temperature into 1°C intervals and compared with observed snowfall at weather stations (Table 3). Observations from nearby Environment and Climate Change Canada weather stations (Pacific Climate Impacts Consortium and PRISM Climate Group 2014) are necessary for comparison because none of the snow-pillow or snow-course observing sites record daily snowfall separately. Precipitation and daily average temperature recorded at the same station are supplied to the snow phase equation for further comparison.

Observed snowfall (Fig. 6, left column) at Whistler and Grouse is close to being normally distributed while Chilliwack snowfall occurrence is skewed left. A significant proportion of daily snowfall occurs when daily average temperature is greater than 0°C (primarily during the latter half of the snow season in spring). When observed precipitation and temperature are used to calculate daily snowfall (Fig. 6, center column), the distributions at Grouse and Whistler are very similar while the asymmetry at observed at Chilliwack is less evident. Daily snowfall from simulated inputs (Fig. 6, right column) results in slightly too frequent snowfall above 0°C at Grouse, and an overestimation of snowfall occurrence above freezing and negative skewness at Whistler and Chilliwack. Too frequent snowfall at warm temperatures likely contributes to the overestimation of annual maximum SWE at Grouse Mountain, Whistler Mountain, and other sites (Fig. 2), as well as causing early accumulation starting dates at most of the snow pillows (Fig. 5). Snow phase models that consider all precipitation above 0°C as rain would miss the contribution from warm temperature snowfall to seasonal snow accumulation, which, based on these stations, could be a significant problem at lower elevations.

c. *Future snow water equivalent*

Future changes in snow water equivalent in the study area are taken from 150-yr (1951–2100) simulations of daily

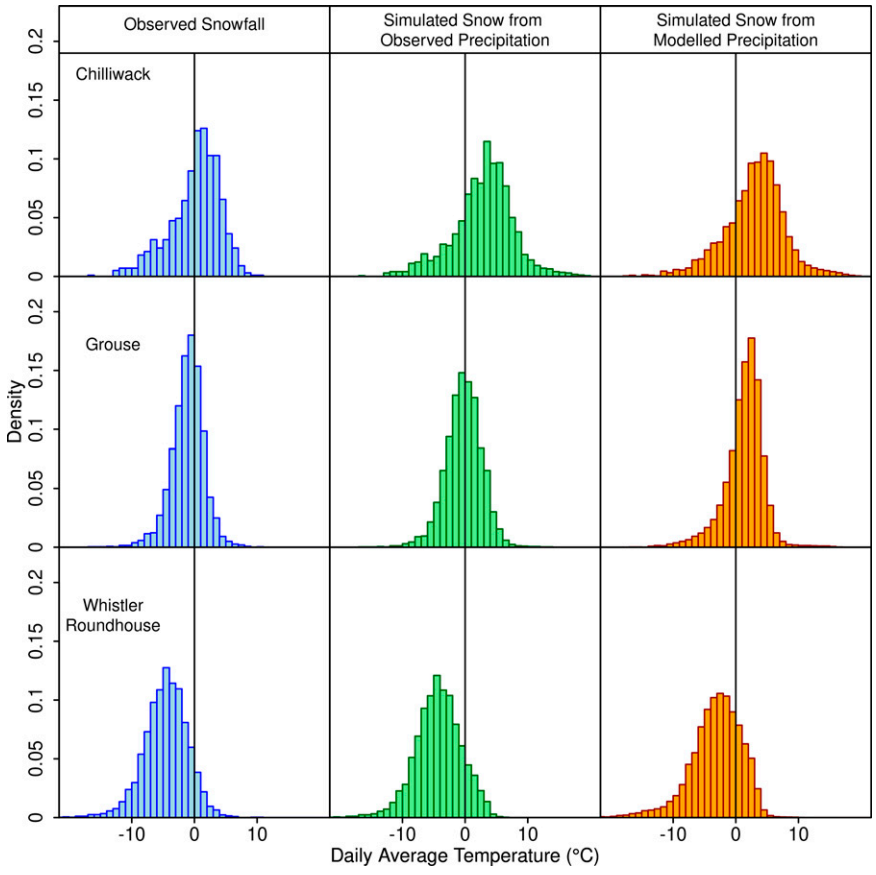

FIG. 6. Observed and simulated snowfall at three weather stations in the study, illustrating the range of temperatures during which snowfall occurs. The bars display histograms of days with snowfall for different daily average temperatures. (left) Snowfall obtained from weather-station observations of temperature and snowfall. (center) Snowfall generated using station observations of temperature and precipitation with the snow phase equation [Eqs. (4) and (5)] to generate snowfall. (right) Snowfall generated using downscaled PNWNAmet temperature and precipitation for each site with the snow phase equation to simulate snowfall.

SWE using inputs from each of the 12 downscaled GCMs. Changes in SWE are presented relative to average temperature changes for the study area. Displaying temperature-dependent results shifts the contribution of scenario uncertainty in SWE from the choice of a selected greenhouse gas concentration pathway (RCP8.5 here) to the timing of when the temperature thresholds are reached. For near-term (next few decades) the uncertainty in the timing of temperature changes is substantially reduced, though it remains a significant factor later in the twenty-first century (Arnell et al. 2019). In each of the 12 downscaled GCMs, annual temperature anomalies (relative to 1981–2010) averaged for the study region are smoothed with a 30-yr moving average. Future periods used to calculate projected changes in SWE are obtained from the 30 years centered on the first year in which the smoothed temperature anomaly reaches 1°, 2°, and 3°C. The ensemble median years (with 10th–90th-percentile ranges) in which each temperature threshold is reached are 2021 (2015–25) for 1°C, 2042 (2032–60) for 2°C, and 2060 (2048–79) for 3°C (Table 4).

Ensemble average percent changes in annual peak SWE for those three levels of future warming are displayed in Fig. 7. At 1°C of warming, most of the region experiences minimal change in peak SWE (less than 10%) except for locations near the ocean and low elevation valleys where historical peak SWE is less than 50 mm on average. As warming increases to 2° and 3°C, reductions in peak SWE are expected to extend both farther inland along valleys, and higher in elevation. With 3°C of warming, lower-level mountains in the southwestern part of the study region (North Shore Mountains, lower Coast Range) are expected to accumulate up to only 50% of peak SWE observed in the past. Such changes in snow conditions will result in impacts for various snow-dependent sectors including winter recreation and water reservoir supply.

1) WHISTLER–BLACKCOMB SKI RESORT

Whistler–Blackcomb Ski Resort is the largest ski resort in Canada, encompassing two mountains, over 1400 m of vertical relief (674–2086 m), and 200 ski runs (Government of Canada

TABLE 4. Years in which the annual average temperature anomaly for the study area reaches 1°, 2°, and 3°C relative to 1981–2010 for each of the 12 GCMs following the RCP8.5 emissions pathway. The years are selected using a 31-yr moving average of the regionally averaged temperature anomalies to reduce interannual variability.

Model	1°C	2°C	3°C
ACCESS1.0	2015	2039	2067
CanESM2	2014	2032	2055
CCSM4	2023	2041	2063
CNRM-CM5	2020	2052	2065
CSIRO Mk3.6.0	2025	2042	2056
GFDL-ESM2G	2024	2051	2071
HadGEM2-CC	2018	2033	2045
HadGEM2-ES	2016	2034	2047
INM-CM4.0	2040	2065	2085
MIROC5	2017	2042	2061
MPI-ESM-LR	2024	2044	2060
MRI-CGCM3	2033	2061	2080
Median	2021	2042	2061

2012). As with other ski resorts in southwestern BC, winter and spring snow amounts are expected to decline with increasing temperatures as a result of climate change (Hewer and Gough 2018; Pidwirny et al. 2018; Scott and McBoyle 2006). Given its more inland location and higher elevation [Whistler Mountain (WM); Fig. 1], Whistler and Blackcomb Mountains are expected to retain higher SWE levels than other lower-elevation ski hills (e.g., North Shore Mountain locations) as temperatures warm. However, SWE amounts on the lower reaches of the mountains extending into Whistler Village are more vulnerable to increasing temperatures. Using the high-resolution projections from the snow model, SWE levels at multiple elevations along the mountain ski runs can be explored in greater detail.

Figure 8 illustrates differences in the robustness of SWE levels to temperature change along the length of ski runs on Whistler Mountain. At about 1800 m and above (Fig. 8, top row) spring (defined as March–May) average SWE levels are expected to see modest declines even at 3°C of warming. Although low SWE levels can occur in any year because of low precipitation, it is only above 4°C of warming that systematic declines are expected. The lower third of the ski hill (between 674 and 950 m) is much more susceptible to temperature increases, with spring SWE expected to decrease to near zero levels at 3°C of warming and spring SWE all but disappearing at the base of the mountain (674 m).

Elevation-dependent results suggest that at, 2°C of warming, 75% of the ski area (above 850 m) of the mountain will still

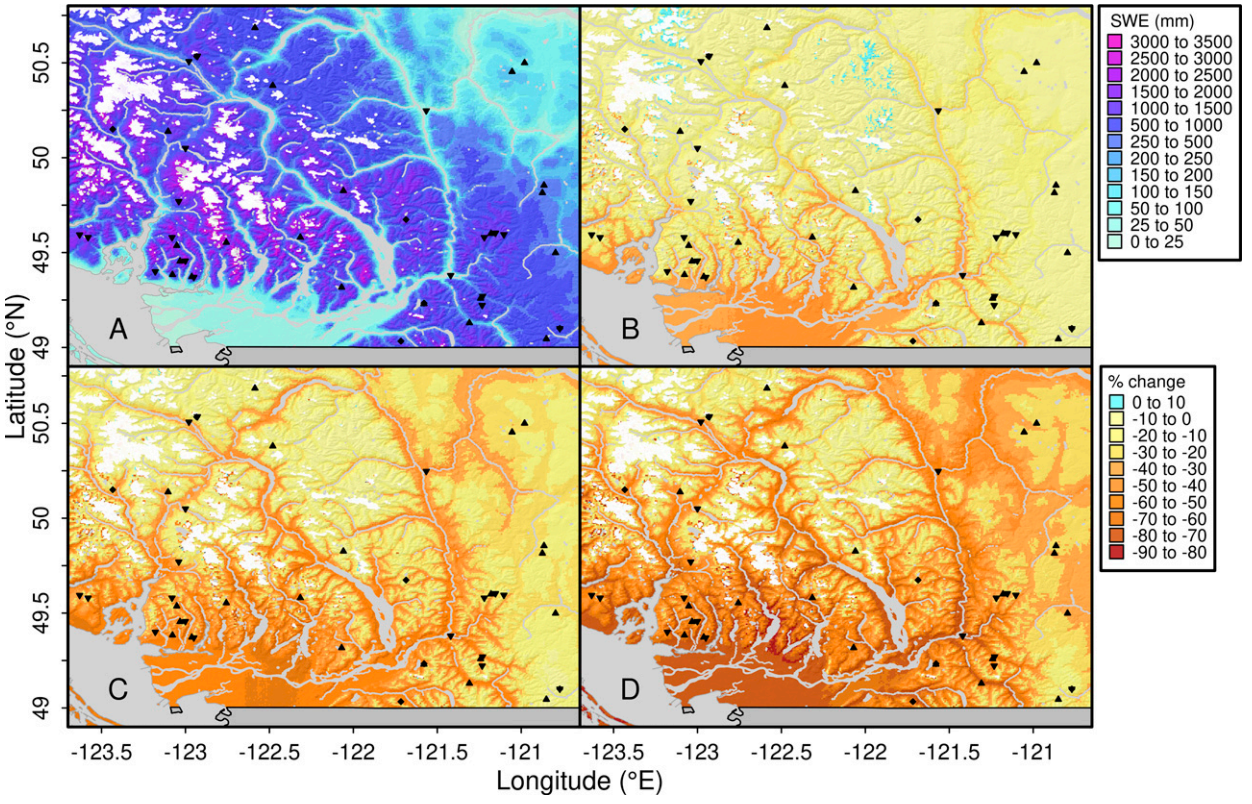

FIG. 7. Past averages and percent changes in future average annual peak SWE for the study area simulated using the ensemble average of the 12 downscaled GCMs: (a) average annual peak SWE during 1951–2012 and percent changes in peak SWE when average annual temperature anomalies for the study area in each model reach (b) 1°, (c) 2°, and (d) 3°C. Future values are based on 30-yr averages centered on the year in which each temperature anomaly is reached, and percent changes are relative to a 1981–2010 average. White regions are glaciated areas, and gray regions are bodies of water, both of which are omitted when calculating summary statistics.

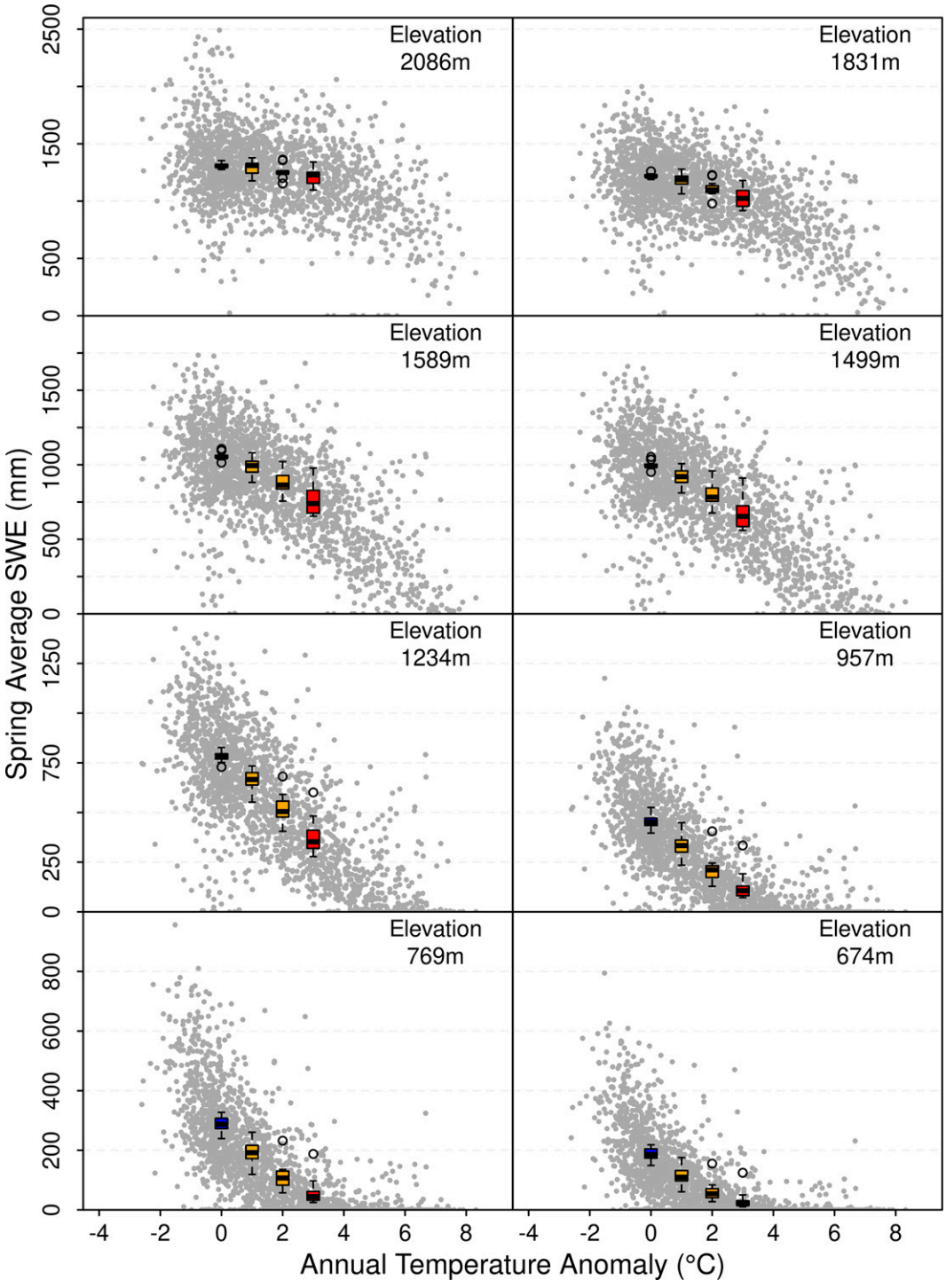

FIG. 8. Average spring SWE at the eight downscaled grid cells from near the top of Whistler mountain (2086 m) to the base of the ski hill (674 m). Spring SWE values are displayed against spring temperature anomalies (relative to 1981–2010) for each year between 1951 and 2100 from the 12 downscaled GCMs (gray dots). Boxplots in each panel represent average spring SWE from each of the 12 GCMs. For each GCM, spring SWE is averaged over the 30 years centered on the year in which the temperature anomalies 1° (yellow), 2° (orange), and 3°C (red) are reached, as well as the historical period 1981–2010 (blue).

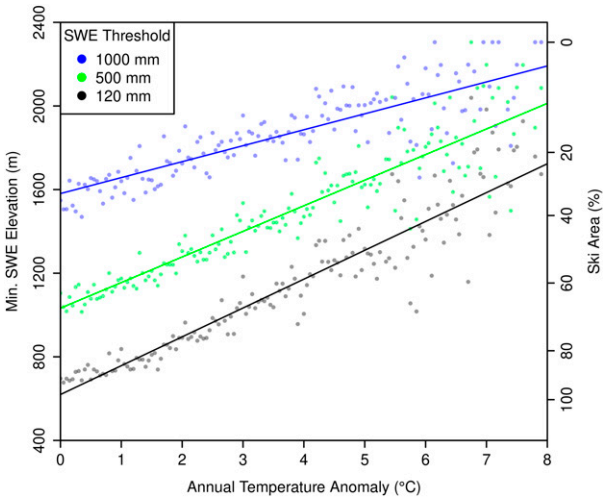

FIG. 9. Elevation at which three different SWE thresholds occur as a function of annual temperature anomaly. Minimum spring average SWE needed for reliable ski operations (120 mm) is shown in black. Spring average SWE are calculated at all downscaled GCM grid cells located within the Whistler–Blackcomb Resort boundary. The percent area of Whistler–Blackcomb Resort encompassed by grid cells above each elevation is displayed on the right-hand plot axis. A linear fit using ordinary least squares to the 120-mm SWE threshold (R^2 = 0.84; RSE = 137 mm) suggests an increase in spring average temperature of 1°C raises the 120-mm SWE level by 140 m. For the 500-mm threshold (R^2 = 0.83; RSE = 122 mm), the rate of increase is 120 m per 1°C increase. For the 1000-mm threshold (R^2 = 0.71; RSE = 109 mm), the rate of increase is 75 m per 1°C increase.

reliably accumulate sufficient SWE levels for skiing (approximately 120 mm spring average SWE; Damm et al. 2017). At 3°C of warming, areas below 1000-m elevation are much more likely to experience low SWE levels that are insufficient for skiing. The elevation at which the 120-mm SWE threshold occurs displays a strong linear dependence on temperature (Fig. 9). If all model grid cells within the Whistler–Blackcomb boundary are considered, for every 1°C increase in spring average temperature, the elevation of the minimum SWE threshold rises by 140 m. A slightly lower elevation rise with temperature occurs for 500-mm SWE levels (120 m per 1°C increase), and elevations with deeper spring snow (1000-mm average spring SWE) rise more slowly with increasing temperature (75 m per 1°C increase). An increase in annual average temperatures of 2°C results in a minimum SWE threshold at about 850-m elevation, which is projected to occur approximately in 2042 (2032–60) based on the median timing of the ensemble temperature anomalies following the high (RCP8.5) emissions pathway.

2) METRO VANCOUVER WATERSHEDS

Metro Vancouver is a large regional district in the southwest of the study area encompassing 23 city or local authorities with a population of 2.5 million. The district receives the majority of its municipal drinking water from three mixed rain–snow watersheds in the North Shore Mountains where replenishment during the summer months is largely dependent on melting snow (Metro Vancouver Water Services 2011). As temperatures warm, peak SWE in the watersheds (commonly used as a measure of stored water available for melting in the summer) is projected to decline by 17% (9%–28%) at 1°C, and by 58% (46%–71%) at 3°C of warming (Figs. 10 and 11). The area of the watersheds covered with SWE (with SWE > 10 mm) on the date of annual maximum SWE is projected to shift from 87% (85%–90%) snow covered during the past to 58% (45%–70%) snow covered at 3°C of warming. As temperatures warm, the snow season (defined as the period when the three-basin average SWE is greater than 10 mm) decreases in length (primarily due to ending earlier) and peaks earlier in the year. At 3°C of warming, the snow season is expected to begin 14 (9–20) days later, peak 27 (15–41) days earlier, end 49 (40–57) days earlier (June instead of August), and last 65 (56–75) fewer days than during historical conditions (Fig. 11). The shift to earlier peak and end dates for SWE in the watersheds, coupled with projected decreases in summer precipitation for the region (Pinna Sustainability 2016), suggests that peak runoff is also likely to occur earlier in the year. Earlier peak and lower total volumes of SWE will likely result in reduced water availability in late summer and early autumn, decreasing the reliability of water stored in snowpack for supplying the reservoirs during this period.

5. Discussion and conclusions

As other studies have noted, evaluation of snow-model performance is made more difficult due to the quality of snow related observations (Kumar et al. 2013). Observations of SWE tend to be recorded less frequently and large fractions of the study area are without recorded SWE observations, meaning available observation sites do not provide a representative sample for the study area as a whole. The spatial distribution of calibration and evaluation sites also differ, with evaluation sites concentrated in the southwest and southeast regions of the domain. Although snow-model performance is better at evaluation sites with higher average SWE (Fig. 2), in the northern half of the study area only two such stations (Tenquille Lake and Whistler Mountain) are present. Further evaluation of the snow model using a spatially distributed SWE observation or reanalysis-based dataset could fill in some of these gaps; however, currently available datasets such as SNODAS have limitations. Large magnitude differences between SNODAS and snow-survey SWE at some of the sites are unexpected given the SNODAS assimilation system incorporates Canadian ground snow observations (Barrett 2003), though only the automated snow-pillow observations appear to have been included. Assimilation frequency of ground observations into SNODAS has been found to be low for sites in the Canada leading to increased bias (Lv et al. 2019).

Higher-resolution meteorological inputs incorporating PRISM climatologies appear to improve but not eliminate the structural differences in downscaled temperature and precipitation at the observation sites. This is evident in the temperature biases at the snow-pillow sites where limited coincident measurements are

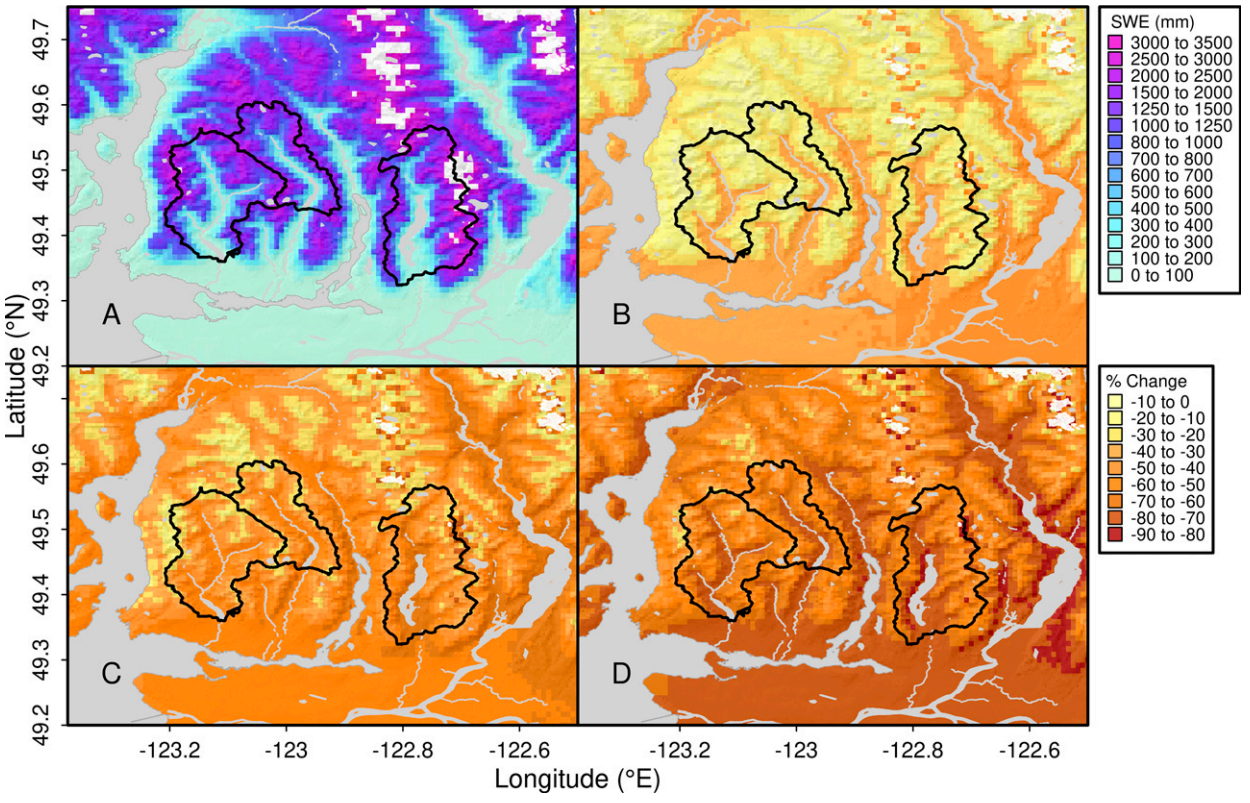

FIG. 10. Past averages and percent changes in future annual peak SWE for the Metro Vancouver municipal drinking water watersheds in the North Shore mountains and the surrounding areas simulated using the 12 downscaled GCMs ensemble average. The three watersheds from left to right in each panel supply the Capilano, Seymour, and Coquitlam reservoirs. Shown are (a) annual peak SWE during 1951–2012 and percent changes in annual peak SWE when average annual temperature anomalies for study area in each GCM reach (b) 1°, (c) 2°, and (d) 3°C. Future values are based on 30-yr averages centered on the year in which each temperature anomaly is reached, and percent changes are relative to a 1981–2010 average. White regions are glaciated areas, and gray regions are bodies of water, both of which are omitted when calculating summary statistics.

available. Good agreement between modeled and observed SWE at Tenquille Lake, Wahleach Lake, Blackwall Peak, and Upper Squamish suggests further improving the input variable fidelity at other sites would decrease SWE bias without necessitating structural changes to the snow model. Extending the analysis to other locations in the province with snow-survey and station data could confirm the magnitude of this effect.

Performance in simulating SWE is also dependent on accurately assigning daily precipitation values as rain or snow. The default Walter snow model splits precipitation at 0°C (Walter et al. 2005), while the current configuration employs a phase equation with calibrated coefficients over the study domain. The revised phase equation allows snow to occur at temperatures above 0°C, which is important for accurately simulating snow levels during the spring season. Allowing phase model parameters to vary temporally (e.g., monthly or seasonally), and be dependent on humidity or other moisture variables could also increase the accuracy of categorizing precipitation at the beginning and end of the snow seasons, particularly in a warming climate (Jennings et al. 2018; Harpold et al. 2017). Calibrating only the phase equation parameters may result in that aspect compensating for deficiencies in other uncalibrated components of the snow model. A more systematic sensitivity analysis of the snow-model components could identify aspects where calibration would be beneficial.

Further improvement in simulating SWE could require more detailed representations of physical processes that are simplified or omitted in the Walter snow model, although at the cost of more complex input data and computing requirements. Individual grid cells in the snow model are spatially uncoupled, and only one snow layer with homogeneous properties is considered. Winds are assumed constant across the domain and are incorporated in the model as heat transfer resistance terms within sensible and latent heat parameterizations. Cloud cover affects only longwave radiation resulting in an overestimation from incoming shortwave, and likely contributes to the shorter lengths and earlier peaks in the snow seasons. Tree canopy is also not explicitly included in the snow model, which omits both the effects on wind, shortwave and longwave radiation, and the interception and sublimation of snowfall. Neglecting interception and sublimation from forest cover likely contributes to the bias of SWE at many of the survey sites (Pomeroy and Brun 2001). Given the importance of wind, radiation, transport, cloud cover, and tree canopy in the high relief areas of the snow model, future

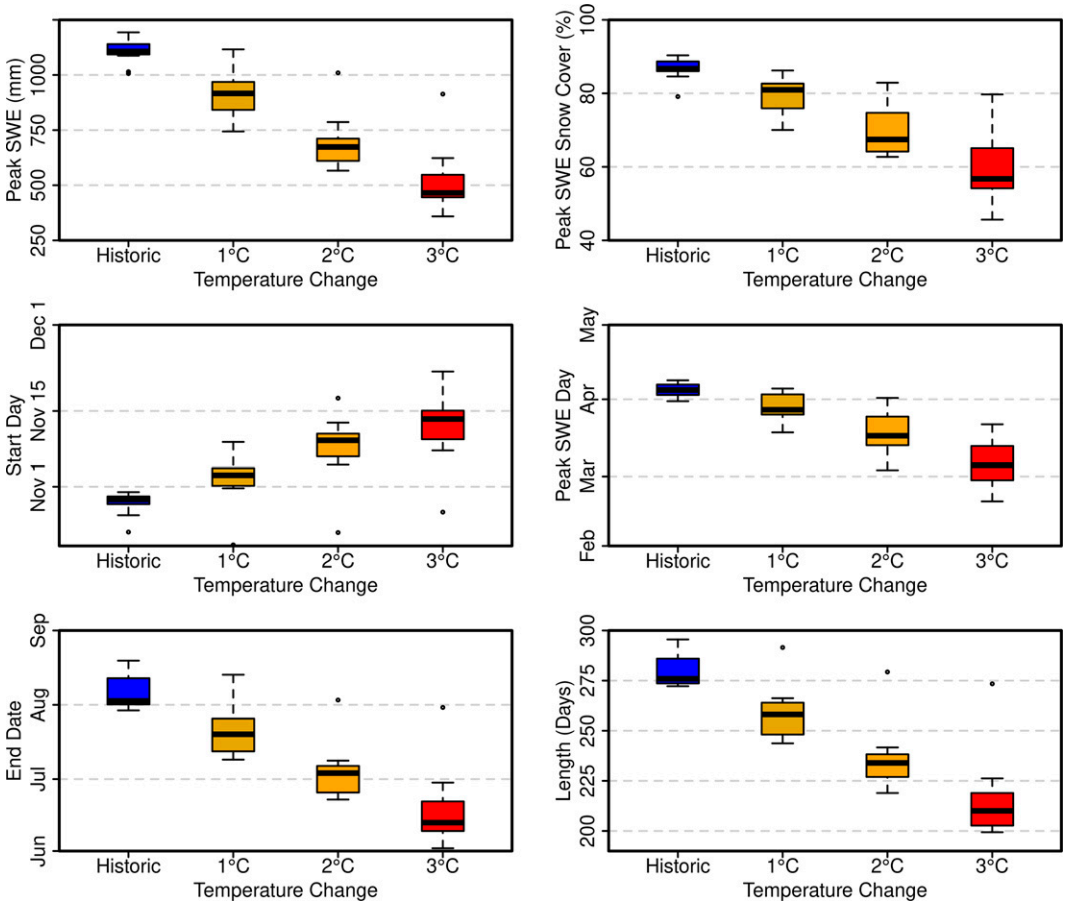

FIG. 11. Average past values and projected changes in annual peak SWE and snow-season timing for the Metro Vancouver watersheds. In the bottom-four snow-timing panels, the snow season is defined as the period when average SWE for the three watersheds is greater than 10 mm. Boxplots in each panel represent results from the 12 GCMs averaged over the 30 years centered on the year in which the temperature anomalies 1° (yellow), 2° (orange), and 3°C (red) are reached, as well as the historical period 1981–2010 (blue). Individual boxplots display the median (central line), interquartile range (central box), 1.5 times the interquartile range (whiskers), and outliers beyond the whiskers (open circles).

work will investigate the inclusion of these aspects in the existing model and comparisons with coupled, multilayer snow models (e.g., SnowModel; Liston and Elder 2006).

Future simulated SWE conditions at Whistler–Blackcomb and the Metro Vancouver watersheds highlight the different sensitivities of snow conditions to future changes at different, relatively nearby locations. Snow water equivalent at mid- to high-elevation areas at Whistler mountain are much more resilient to future changes than the lower elevation valleys within the watersheds. Similar patterns occur across the study area. Declines in SWE result primarily from increasing temperatures as precipitation is projected to increase modestly (<10%) in seasons outside of summer, where already low precipitation is projected to decline (Pinna Sustainability 2016). For processes dependent on melting water stored in snowpack, the combination of warmer, drier summers with shorter snow seasons and reduced SWE volume has implications for water availability. Earlier snow-season end dates in the watersheds and other similar basins means the timing of when signification precipitation in autumn resumes to replace melting SWE becomes more important. Further investigation with a hydrologic model is needed to determine how long such decreased runoff could persist during these periods.

While regions away from the ocean and at higher elevations continue to maintain reliable if reduced SWE accumulation with warming temperatures, at 3°C temperature increase areas within the study that accumulate SWE consistently are substantially reduced. Transition zones with mixed rain and snow are expected to move upward in elevation with increasing temperatures. Reduced areas of SWE accumulation means years with below average precipitation could result in substantially less stored water in snowpack than during similar years in the past. Earlier loss of snow cover over more of the study area could also increase forest fire risk through reduced soil moisture, though increased spring precipitation may offset this effect. Existing adaptation steps to reduced SWE such as installing snowmaking infrastructure at Whistler–Blackcomb and increasing water storage capacity in the Metro Vancouver watersheds may need to be expanded in the future as temperatures continue to warm.

TABLE A1. Site name and elevation information for the manual snow-survey (snow course) observational sites used to calibrate and evaluate the snow model. Calibration sites on the left are used both to calibrate and to evaluate the snow model, whereas evaluation sites on the right are used only to evaluate the snow model. Map symbols are used to identify sites in Fig. 1.

Calibration sites			Evaluation sites		
Site name	Map symbol	Elev (m)	Site name	Map symbol	Elev (m)
Brookmere	BR	994	Blackwall Peak	BP	1940
Callaghan	CG	1009	Boston Bar Lower	BL	1230
Dickson Lake	DL	1147	Boston Bar Upper	BU	1340
Disappointment Lake	DI	1050	Burwell	BW	880
Dog Mountain	DM	1080	Chapman Creek	CC	1020
Duffey Lake	DU	1200	Cornwall Hills	CH	2000
Gnawed Mountain	GM	1580	Diamond Head	DH	1420
Great Bear	GB	1660	Edwards Lake	EL	1070
Grouse Mountain	GR	1126	Hollyburn	HB	1100
Hamilton Hill	HH	1477	Hope	HO	70
Highland Valley	HV	1550	Loch Lomond	BL	900
Klesilkwa	KL	1130	Lytton	LY	270
Lightning Lake	LL	1254	Mount Seymour	MS	1070
McGillivray Pass	MP	1725	New Tashme	NT	700
Nahatlatch	NA	1530	Ottomite	OT	1460
Orchid Lake	OL	1178	Pavilion Mountain	PM	1960
Palisade Lake	PL	898	Sumallo River	SR	880
Shovelnose Mountain	SM	1456	Tenquille Lake	TQ	1680
Stave Lake	SL	1211	Whistler Mountain	WM	1450
Sumallo River West	SW	790	Wolverine Creek	WC	250
Wahleach	WA	1400			

Effectively modeling daily snow water equivalent in areas of mountainous terrain can often require extensive calibration efforts, or complex and computationally expensive systems. A process-based energy balance model offers a potentially simpler and faster means of simulating SWE. Applying the Walter snow model supplied with recent, high-resolution meteorological inputs to southwestern British Columbia yields effective performance in replicating SWE interannual variability, but room for improvement remains. Biases in simulated SWE occur where differences in temperature and precipitation persist between observations and the meteorological inputs. Increased spatial resolution in this snow-modeling approach allows for more detailed exploration of spatial- and elevation-dependent responses of accumulated SWE to climate change. With improvements to simulated precipitation and further verification, this method could provide a useful benchmark for other more complex methods of simulating accumulated snowfall.

Acknowledgments. ERA5 reanalysis data were generated using information from the Copernicus Climate Change Service (2017); F. W. Zwiers, F. Anslow, and C. L. Curry and three anonymous reviewers provided helpful comments that improved the paper, and D. L. Spittlehouse provided helpful suggestions at the early stages of this work.

Data availability statement. Observations of snow water equivalent were obtained from the BC Ministry of Environment and Climate Change Strategy (BC Ministry of Environment and Climate Change Strategy 2015; https://www2.gov.bc.ca/gov/content/environment/air-land-water/water/water-science-data/water-data-tools/snow-survey-data). Reanalysis snow water equivalent was obtained from NOAA's Snow Data Assimilation System (National Operational Hydrologic Remote Sensing Center 2004; Barrett 2003; https://nsidc.org/data/G02158). Stage one of the statistical downscaling method employing BCCAQv2 (Werner and Cannon 2016; Cannon et al. 2015) was performed using the R package "ClimDown" (Hiebert et al. 2018). Global climate model simulations of daily precipitation, maximum temperature, and minimum temperature (appendix B) were obtained from the Earth System Grid Federation data portal (Williams et al. 2009). A repository containing the R code used for the second downscaling stage is available via GitHub (https://github.com/pacificclimate/monthlyDS). The gridded observational data used in the calibration and evaluation of the downscaled GCMs are available via the Pacific Climate Impacts Consortium Data Portals. PNWNAmet (Werner et al. 2019) is available at https://pacificclimate.org/data/daily-gridded-meteorological-datasets. PRISM (Daly et al. 2008) data are available at https://pacificclimate.org/data/prism-climatology-and-monthly-timeseries-portal.

TABLE A2. Site name and elevation information for the ASP observational sites used to calibrate and evaluate the snow model. Map symbols are used to identify sites in Fig. 1.

Site name	Map symbol	Elev (m)
Blackwall Peak	BP	1940
Chilliwack River	CR	1601
Spuzzum Creek	SC	1197
Tenquille Lake	TQ	1680
Upper Squamish	US	1340
Wahleach Lake	WL	1400

TABLE B1. The list of 12 GCMs used in this analysis. Twelve GCMs are selected from the CMIP5 set of available GCMs that are most representative of the larger ensemble. Among all available CMIP5 GCMs considered in the selection, some GCMs provide multiple simulations (realizations) using the same climate model. The selected simulation from each GCM is indicated with the realization identifier, which denotes the realization *r*, initialization *i*, and physics *p* version numbers.

Model	Realization	Spatial resolution	Institution
ACCESS1.0	r1i1p1	1.25° × 1.87°	CSIRO–BOM
CanESM2	r1i1p1	1.25° × 0.94°	CCCMA
CCSM4	r2i1p1	1.25° × 0.94°	NCAR
CNRM-CM5	r1i1p1	1.40° × 1.40°	CNRM
CSIRO Mk3.6.0	r1i1p1	1.87° × 1.87°	CSIRO
GFDL-ESM2G	r1i1p1	2.50° × 2.00°	GFDL
HadGEM2-CC	r1i1p1	1.87° × 1.24°	Met Office Hadley Centre
HadGEM2-ES	r1i1p1	1.87° × 1.24°	Met Office Hadley Centre
INM-CM4.0	r1i1p1	1.50° × 2.00°	INM
MIROC5	r3i1p1	1.40° × 1.40°	MIROC
MPI-ESM-LR	r3i1p1	1.87° × 1.87°	MPI
MRI-CGCM3	r1i1p1	1.12° × 1.12°	MRI

APPENDIX A

Snow Observation Sites

Site names, map symbols, and site elevations are given here for the snow-survey (Table A1) and snow-pillow (Table A2) locations.

APPENDIX B

Global Climate Models

Table B1 lists the 12 GCMs used in this analysis. More information on the full model and institution names can be found online (https://www.ametsoc.org/PubsAcronymList).

REFERENCES

Arnell, N. W., J. A. Lowe, A. J. Challinor, and T. J. Osborn, 2019: Global and regional impacts of climate change at different levels of global temperature increase. *Climatic Change*, **155**, 377–391, https://doi.org/10.1007/s10584-019-02464-z.

Barnett, T. P., J. C. Adam, and D. P. Lettenmaier, 2005: Potential impacts of a warming climate on water availability in snow-dominated regions. *Nature*, **438**, 303–309, https://doi.org/10.1038/nature04141.

Barrett, A., 2003: National Operational Hydrologic Remote Sensing Center Snow Data Assimilation System (SNODAS) products at NSIDC. NSIDC Special Rep. 11, 19 pp., https://nsidc.org/sites/nsidc.org/files/files/nsidc_special_report_11.pdf.

BC Ministry of Environment and Climate Change Strategy, 2015: Snow survey data. BC River Forecast Centre, accessed 26 February 2020, https://www2.gov.bc.ca/gov/content/environment/air-land-water/water/water-science-data/water-data-tools/snow-survey-data.

Bormann, K. J., J. P. Evans, and M. F. McCabe, 2014: Constraining snowmelt in a temperature-index model using simulated snow densities. *J. Hydrol.*, **517**, 652–667, https://doi.org/10.1016/j.jhydrol.2014.05.073.

Cannon, A. J., 2014: Selecting GCM scenarios that span the range of changes in a multimodel ensemble: Application to CMIP5 climate extremes indices. *J. Climate*, **28**, 1260–1267, https://doi.org/10.1175/JCLI-D-14-00636.1.

——, S. R. Sobie, and T. Q. Murdock, 2015: Bias correction of GCM precipitation by quantile mapping: How well do methods preserve changes in quantiles and extremes? *J. Climate*, **28**, 6938–6959, https://doi.org/10.1175/JCLI-D-14-00754.1.

Copernicus Climate Change Service, 2017: ERA5: Fifth generation of ECMWF atmospheric reanalyses of the global climate. Accessed 11 March 2020, https://cds.climate.copernicus.eu/cdsapp#!/home.

Curry, C. L., and F. W. Zwiers, 2018: Examining controls on peak annual streamflow and floods in the Fraser River basin of British Columbia. *Hydrol. Earth Syst. Sci.*, **22**, 2285–2309, https://doi.org/10.5194/hess-22-2285-2018.

Dai, A., 2008: Temperature and pressure dependence of the rain-snow phase transition over land and ocean. *Geophys. Res. Lett.*, **35**, L12802, https://doi.org/10.1029/2008GL033295.

Daly, C., M. Halbleib, J. I. Smith, W. P. Gibson, M. K. Doggett, G. H. Taylor, J. Curtis, and P. P. Pasteris, 2008: Physiographically sensitive mapping of climatological temperature and precipitation across the conterminous United States. *Int. J. Climatol.*, **28**, 2031–2064, https://doi.org/10.1002/joc.1688.

Damm, A., W. Greuell, O. Landgren, and F. Prettenthaler, 2017: Impacts of +2°C global warming on winter tourism demand in Europe. *Climate Serv.*, **7**, 31–46, https://doi.org/10.1016/j.cliser.2016.07.003.

Frei, P., S. Kotlarski, M. A. Liniger, and C. Schär, 2018: Future snowfall in the Alps: Projections based on the EURO-CORDEX regional climate models. *Cryosphere*, **12** (1), 1–24, https://doi.org/10.5194/tc-12-1-2018.

Fuka, D. R., M. T. Walter, J. A. Archibald, T. S. Steenhuis, and Z. M. Easton, 2018: EcoHydRology: A community modeling foundation for eco-hydrology. R package, https://CRAN.R-project.org/package=EcoHydRology.

Garen, D. C., and D. Marks, 2005: Spatially distributed energy balance snowmelt modelling in a mountainous river basin: Estimation of meteorological inputs and verification of model results. *J. Hydrol.*, **315**, 126–153, https://doi.org/10.1016/j.jhydrol.2005.03.026.

Gergel, D. R., B. Nijssen, J. T. Abatzoglou, D. P. Lettenmaier, and M. R. Stumbaugh, 2017: Effects of climate change on snowpack and fire potential in the western USA. *Climatic*

Change, **141**, 287–299, https://doi.org/10.1007/s10584-017-1899-y.

Government of Canada, 2012: Facing the elements: Building business resilience in a changing climate. Whistler-Blackcomb Holdings, Inc., National Round Table on the Environment and the Economy Advisory Rep., 136 pp., https://issuu.com/nrtee/docs/cp5-advisory-report.

Harpold, A. A., S. Rajagopal, J. B. Crews, T. Winchell, and R. Schumer, 2017: Relative humidity has uneven effects on shifts from snow to rain over the western U.S. *Geophys. Res. Lett.*, **44**, 9742–9750, https://doi.org/10.1002/2017GL075046.

Hersbach, H., and Coauthors, 2018: Operational global reanalysis: Progress, future directions and synergies with NWP. ERA Rep. Series 27, 63 pp., https://www.ecmwf.int/node/18765.

Hewer, M. J., and W. A. Gough, 2018: Thirty years of assessing the impacts of climate change on outdoor recreation and tourism in Canada. *Tourism Manage. Perspect.*, **26**, 179–192, https://doi.org/10.1016/j.tmp.2017.07.003.

Hiebert, J., A. Cannon, T. Murdock, S. Sobie, and A. Werner, 2018: ClimDown: Climate downscaling in R. *J. Open Source Software*, **3**, 360, https://doi.org/10.21105/joss.00360.

Hunter, R. D., and R. K. Meentemeyer, 2005: Climatologically aided mapping of daily precipitation and temperature. *J. Appl. Meteor.*, **44**, 1501–1510, https://doi.org/10.1175/JAM2295.1.

Il Jeong, D., and L. Sushama, 2018: Rain-on-snow events over North America based on two Canadian regional climate models. *Climate Dyn.*, **50**, 303–316, https://doi.org/10.1007/s00382-017-3609-x.

Jennings, K. S., T. S. Winchell, B. Livneh, and N. P. Molotch, 2018: Spatial variation of the rain–snow temperature threshold across the Northern Hemisphere. *Nat. Commun.*, **9**, 1148, https://doi.org/10.1038/s41467-018-03629-7.

Kumar, M., D. Marks, J. Dozier, M. Reba, and A. Winstral, 2013: Evaluation of distributed hydrologic impacts of temperature-index and energy-based snow models. *Adv. Water Resour.*, **56**, 77–89, https://doi.org/10.1016/j.advwatres.2013.03.006.

Liston, G. E., and K. Elder, 2006: A distributed snow-evolution modeling system (SnowModel). *J. Hydrometeor.*, **7**, 1259–1276, https://doi.org/10.1175/JHM548.1.

Liu, C., and Coauthors, 2017: Continental-scale convection-permitting modeling of the current and future climate of North America. *Climate Dyn.*, **49**, 71–95, https://doi.org/10.1007/s00382-016-3327-9.

Luo, C., 2017: The CLEVER model: A real-time flood forecasting model for British Columbia. BC River Forecast Centre Tech. Rep., 34 pp.

Lv, Z., J. W. Pomeroy, and X. Fang, 2019: Evaluation of SNODAS snow water equivalent in western Canada and assimilation into a cold region hydrological model. *Water Resour. Res.*, **55**, 11 166–11 187, https://doi.org/10.1029/2019WR025333.

Maraun, D., 2013: Bias correction, quantile mapping, and downscaling: Revisiting the inflation issue. *J. Climate*, **26**, 2137–2143, https://doi.org/10.1175/JCLI-D-12-00821.1.

Marks, D., J. Domingo, D. Susong, T. Link, and D. Garen, 1999: A spatially distributed energy balance snowmelt model for application in mountain basins. *Hydrol. Processes*, **13**, 1935–1959, https://doi.org/10.1002/(SICI)1099-1085(199909)13:12/13<1935::AID-HYP868>3.0.CO;2-C.

Metro Vancouver Water Services, 2011: Drinking water management plan. Metro Vancouver Tech. Rep., 22 pp., http://www.metrovancouver.org/services/water/WaterPublications/DWMP-2011.pdf.

Morrison, J., M. C. Quick, and M. G. G. Foreman, 2002: Climate change in the Fraser River watershed: Flow and temperature projections. *J. Hydrol.*, **263**, 230–244, https://doi.org/10.1016/S0022-1694(02)00065-3.

Mudryk, L. R., C. Derksen, P. J. Kushner, and R. Brown, 2015: Characterization of Northern Hemisphere snow water equivalent datasets, 1981–2010. *J. Climate*, **28**, 8037–8051, https://doi.org/10.1175/JCLI-D-15-0229.1.

Municipality of Whistler, 2016: Community energy and climate action plan. Resort Municipality of Whistler Tech. Rep., 110 pp., https://www.whistler.ca/sites/default/files/2021/Sep/related/27498/cecap.0_final.pdf.

National Operational Hydrologic Remote Sensing Center, 2004: Snow data assimilation system (SNODAS) data products at NSIDC, version 1. Accessed 13 March 2020, https://nsidc.org/data/G02158.

Nychka, D., R. Furrer, J. Paige, S. Sain, F. Gerber, M. Iverson, and University Corporation for Atmospheric Research, 2017: fields: Tools for spatial data. R package, UCAR, https://github.com/dnychka/fieldsRPackage.

Ohmura, A., 2001: Physical basis for the temperature-based melt-index method. *J. Appl. Meteor.*, **40**, 753–761, https://doi.org/10.1175/1520-0450(2001)040<0753:PBFTTB>2.0.CO;2.

Pacific Climate Impacts Consortium and PRISM Climate Group, 2014: High resolution PRISM climatology. PCIC, accessed 4 May 2020, https://www.pacificclimate.org/data/prism-climatology-and-monthly-timeseries-portal.

Pidwirny, M., K. Bahbahani, and S. Pederson, 2018: Climate change challenges for alpine ski resorts in western Canada. *Alpine Club of Canada's State of the Mountains Report*, L. Parrott, Z. Robinson, and D. Hik, Eds., Alpine Club of Canada, 16–18, https://www.stateofthemountains.ca/reports.

Pinna Sustainability, 2016: Climate projections for metro Vancouver. Metro Vancouver Tech. Rep., 80 pp., http://www.metrovancouver.org/services/air-quality/AirQualityPublications/ClimateProjectionsForMetroVancouver.pdf.

Pomeroy, J. W., and E. Brun, 2001: Physical properties of snow. *Snow Ecology*, H. G. Jones et al., Eds., Cambridge University Press, 45–126.

——, D. M. Gray, T. Brown, N. R. Hedstrom, W. L. Quinton, R. J. Granger, and S. K. Carey, 2007: The cold regions hydrological model: A platform for basing process representation and model structure on physical evidence. *Hydrol. Processes*, **21**, 2650–2667, https://doi.org/10.1002/hyp.6787.

Riahi, K., and Coauthors, 2011: RCP 8.5—A scenario of comparatively high greenhouse gas emissions. *Climatic Change*, **109**, 33, https://doi.org/10.1007/s10584-011-0149-y.

Rutter, N., and Coauthors, 2009: Evaluation of forest snow processes models (SnowMIP2). *J. Geophys. Res.*, **114**, D06111, https://doi.org/10.1029/2008JD011063.

Scott, D., and G. McBoyle, 2006: Climate change adaptation in the ski industry. *Mitigation Adapt. Strategies Global Change*, **12**, 1411, https://doi.org/10.1007/s11027-006-9071-4.

Snauffer, A. M., W. W. Hsieh, A. J. Cannon, and M. A. Schnorbus, 2018: Improving gridded snow water equivalent products in British Columbia, Canada: Multi-source data fusion by neural network models. *Cryosphere*, **12**, 891–905, https://doi.org/10.5194/tc-12-891-2018.

Sobie, S. R., and T. Q. Murdock, 2017: High-resolution statistical downscaling in southwestern British Columbia. *J. Appl.*

Meteor. Climatol., **56**, 1625–1641, https://doi.org/10.1175/JAMC-D-16-0287.1.

Sproles, E., A. W. Nolin, K. Rittger, and T. H. Painter, 2013: Climate change impacts on maritime mountain snowpack in the Oregon Cascades. *Hydrol. Earth Syst. Sci.*, **17**, 2581–2597, https://doi.org/10.5194/hess-17-2581-2013.

Taylor, K. E., R. J. Stouffer, and G. A. Meehl, 2011: An overview of CMIP5 and the experiment design. *Bull. Amer. Meteor. Soc.*, **93**, 485–498, https://doi.org/10.1175/BAMS-D-11-00094.1.

U.S. Army Corps of Engineers, 1998: Runoff from snowmelt. U.S. Army Corps of Engineers Engineer Manual EM 1110-2-1406 (update), 142 pp., https://www.publications.usace.army.mil/Portals/76/Publications/EngineerManuals/EM_1110-2-1406.pdf.

Walter, M., E. S. Brooks, D. K. McCool, L. G. King, M. Molnau, and J. Boll, 2005: Process-based snowmelt modeling: Does it require more input data than temperature-index modeling? *J. Hydrol.*, **300**, 65–75, https://doi.org/10.1016/j.jhydrol.2004.05.002.

Werner, A. T., and A. J. Cannon, 2016: Hydrologic extremes—An intercomparison of multiple gridded statistical downscaling methods. *Hydrol. Earth Syst. Sci.*, **20**, 1483–1508, https://doi.org/10.5194/hess-20-1483-2016.

——, M. A. Schnorbus, R. R. Shrestha, A. J. Cannon, F. W. Zwiers, G. Dayon, and F. Anslow, 2019: A long-term, temporally consistent, gridded daily meteorological dataset for northwestern North America. *Sci. Data*, **6**, 180299, https://doi.org/10.1038/sdata.2018.299.

Williams, D. N., and Coauthors, 2009: The Earth System Grid: Enabling access to multimodel climate simulation data. *Bull. Amer. Meteor. Soc.*, **90**, 195–206, https://doi.org/10.1175/2008BAMS2459.1.